

Article

Preparation of Halloysite/Ag₂O Nanomaterials and Their Performance for Iodide Adsorption

Wenlin Yu ^{1,2}, Qinpeng Dong ^{1,2}, Wenbin Yu ^{2,3,*} , Zonghua Qin ^{2,3}, Xin Nie ^{2,3}, Quan Wan ^{2,3,4}  and Xiuli Chen ^{1,*}

¹ Key Laboratory of Nonferrous Materials and New Processing Technology (Ministry of Education), School of Materials Science and Engineering, Guilin University of Technology, Guilin 541004, China; wenlinyu@glut.edu.cn (W.Y.); Dongqp023@163.com (Q.D.)

² State Key Laboratory of Ore Deposit Geochemistry, Institute of Geochemistry, Chinese Academy of Sciences, Guizhou 550081, China; qinzonghua@mail.gyig.ac.cn (Z.Q.); niexin@mail.gyig.ac.cn (X.N.); wanquan@vip.gyig.ac.cn (Q.W.)

³ University of Chinese Academy of Sciences, Beijing 100049, China

⁴ CAS Center for Excellence in Comparative Planetology, Hefei 230026, China

* Correspondence: yuwenbin@mail.gyig.ac.cn (W.Y.); cxlnwpu@163.com (X.C.)

Abstract: Halloysite/Ag₂O (Hal/Ag₂O) nanomaterials were prepared by growing Ag₂O nanoparticles on the surface of nanotubular halloysite using silver nitrate solution under alkaline conditions. The nanomaterials were characterized by X-ray diffraction (XRD), transmission electron microscopy (TEM), and N₂ adsorption. Good dispersion of Ag₂O nanoparticles with average sizes of 6.07 ± 2.5 nm and 8.04 ± 3.8 nm was achieved in the nanomaterials when using different concentrations of alkali. The nanomaterial with 6.36% Ag₂O (Hal/Ag₂O-2) exhibited rapid adsorption to iodide (I⁻); adsorption equilibrium can be reached within 100 min. The adsorption capacity of I⁻ on Hal/Ag₂O-2 is 57.5 mg/g, which is more than 143 times higher than that of halloysite. The nanomaterial also showed a better adsorption capacity per unit mass of Ag₂O due to the better dispersion and less coaggregation of Ag₂O in the nanomaterial than in the pure Ag₂O nanoparticles. Importantly, Hal/Ag₂O-2 exhibited high selectivity for I⁻, and its I⁻ removal efficiency was hardly affected by the coexistence of Cl⁻, Br⁻, or SO₄²⁻, as well as the initial pH of the solution. With an excellent adsorption performance, the prepared Hal/Ag₂O nanomaterial could be a new and efficient adsorbent capable of the adsorption of radioactive I⁻ from aqueous solution.

Keywords: radionuclides; iodide; nanotube; halloysite; Ag₂O; nanomaterial; adsorption



Citation: Yu, W.; Dong, Q.; Yu, W.; Qin, Z.; Nie, X.; Wan, Q.; Chen, X. Preparation of Halloysite/Ag₂O Nanomaterials and Their Performance for Iodide Adsorption. *Minerals* **2022**, *12*, 304. <https://doi.org/10.3390/min12030304>

Academic Editor: Andrey G. Kalinichev

Received: 17 January 2022

Accepted: 23 February 2022

Published: 27 February 2022

Publisher's Note: MDPI stays neutral with regard to jurisdictional claims in published maps and institutional affiliations.



Copyright: © 2022 by the authors. Licensee MDPI, Basel, Switzerland. This article is an open access article distributed under the terms and conditions of the Creative Commons Attribution (CC BY) license (<https://creativecommons.org/licenses/by/4.0/>).

1. Introduction

With the development of nuclear energy, large amounts of radionuclides (such as ¹²⁹I, ¹³¹I, ¹³⁷Cs, ²³⁸U, ²³⁹Pu, and ²⁴¹Am) are produced and inevitably released into the natural environment, posing a serious threat to public health and environmental protection [1,2]. Among them, radioactive iodine is of the greatest environmental concern because of its high mobility and long half-life [3]. The high mobility of iodine is primarily due to its anionic nature in aqueous environments. It exists as iodide (I⁻) and iodate (IO₃⁻), depending on the redox conditions and pH [4], both of which are repulsed from the negative surface charges on most sediments and minerals. Of these two species, I⁻ is more commonly found in the natural environment with suboxic to reducing conditions and a pH of approximately 4–10 [5]. The half-life of ¹²⁹I is 1.6 × 10⁷ years [6], so ¹²⁹I released into the environment poses a long-term risk to humans and the environment. Exposure to even slight amounts of radioactive iodine could lead to a rise in diseases, such as mental retardation, metabolic disorders, and thyroid cancer [7]. Therefore, the efficient elimination and solidification of radioactive iodine, especially iodide, are important tasks.

In recent decades, different methods, such as adsorption [8–11], oxidation [12], photocatalysis [13], and membrane electrolysis [14], have been used to eliminate radioactive I^- from nuclear wastewater. Of these methods, adsorption has been extensively explored and demonstrated to be the most applicable technology due to the system's flexibility, high elimination efficiency, and low energy input [5,15,16]. For the adsorption method, the adsorbent is a critically important factor affecting the removal efficiency. Many materials, such as activated carbon [17], natural minerals [5,18], metal compounds [19,20], and Ag_2O composites [21], have been used as adsorbents. Remarkably, Ag_2O composites featuring Ag_2O nanoparticles loaded on the surface of different supports are very attractive because of the strong affinity between iodide and silver. Titanate nanofibers/nanotubes [22], nanolaminas [21], and TiO_2 3D spheres [13] have been reported to support Ag_2O , and the generated composites showed excellent adsorption performance for I^- . However, for all these composites, the supports should be synthesized first, making the preparation process of the Ag_2O composites costly and cumbersome.

Halloysite is a naturally occurring dioctahedral 1:1 clay mineral with a unique nanotubular morphology that is inexpensive and easily available worldwide [23]. The nanotubular morphology of halloysite results from the wrapping of the structural layers, and the wrapping process is driven by the lattice mismatch between the adjacent octahedral AlO_6 sheets and tetrahedral SiO_4 sheets [24]. For each halloysite nanotube, the internal surface consists of a gibbsite-like array of aluminol (Al-OH) groups, whereas the external surface is composed of siloxane (Si-O-Si) groups. Generally, the external diameter of halloysite nanotubes ranges from ca. 30 to 190 nm, and the internal diameter ranges from ca. 10 to 100 nm [25]. With these nanoscale dimensions, halloysite possesses a high specific surface area and pore volume, which are advantageous, as well as natural availability, low cost, and environmental compatibility, making halloysite an ideal support for the preparation of composites. In previous works, different nanoparticles/molecules, such as Fe_3O_4 , MnO_x , TiO_2 , Ag, Au, enzymes, etc. [26–30], were supported onto halloysite to prepare composites that have superior adsorption, catalysis, and release performance. However, to the best of our knowledge, there are few reports on supporting Ag_2O on the external surface of halloysite to remove radioactive I^- .

Consequently, this work aimed to prepare halloysite/ Ag_2O nanomaterials by supporting Ag_2O on the surface of halloysite and to assess the feasibility of applying the prepared nanomaterials for the removal of I^- from aqueous solutions. The results indicated that the Ag_2O nanoparticles in the nanomaterial existed primarily on the external surface of the halloysite, with better dispersion and less coaggregation than the unsupported nanoparticles. The halloysite/ Ag_2O nanomaterial exhibited fast kinetics, high adsorption capacity, and selectivity for radioactive I^- , enabling its promising application for radioactive pollution control. The fundamental knowledge derived from this study is also important for the development of new efficient adsorbents based on halloysite in the future.

2. Materials and Methods

2.1. Materials and Chemicals

Raw halloysite was collected from Dafang, Guizhou Province, China. The raw halloysite was purified by manual selection to remove impurities, and the chemical composition (wt%) of the purified halloysite was: SiO_2 , 45.13; Al_2O_3 , 38.09; Fe_2O_3 , 0.19; MgO , 0.06; Na_2O , 0.08; K_2O , 0.05; P_2O_5 , 0.02; TiO_2 , 0.03; and loss, 16.60. The purified halloysite sample was dried overnight at 120 °C and ground, and the resulting powder sample is referred to herein as Hal.

Analytical grade reagents such as $AgNO_3$ and $NaOH$ were used for the synthesis of Ag_2O . KCl , KBr , and K_2SO_4 were AR grade and, in addition to 68.0% HNO_3 , were purchased from Sinopharm Chemical Reagent Co., Ltd. Nonradioactive KI (Sigma-Aldrich, St. Louis, MO, USA) was used as the source of I^- in the adsorption experiments because it has the same chemical reaction properties as radioactive iodine [31,32]. All chemicals were

used as received, without further purification. Deionized water (resistivity, 18.2 M Ω -cm) was used in all of the experiments.

2.2. Preparation of Halloysite/Ag₂O Nanomaterials

Halloysite/Ag₂O nanomaterials were prepared using the following procedures: Hal powder and a 0.1 mol/L AgNO₃ solution with a solid/solution ratio of 1 g/100 mL were placed into a conical flask, and then the suspension was stirred at 700 rpm for 2 h. Then, 10 mL of a NaOH solution with the designated concentration was added dropwise into the conical flask using a peristaltic pump at a flow rate of 0.1 mL/min while vigorously stirring the suspension. After stirring for 8 h, the solid was collected and washed thrice with 15 mL deionized water, and then dried at 80 °C overnight, to yield the halloysite/Ag₂O nanomaterial. Specifically, 0.01 mol/L and 0.05 mol/L NaOH solutions were used to prepare the halloysite/Ag₂O nanomaterials, and the obtained nanomaterials were denoted Hal/Ag₂O-1 and Hal/Ag₂O-2, respectively. Pure Ag₂O nanoparticles (denoted as Ag₂O-NPS) were also prepared for comparative purposes, and its preparation procedure was reported in our previous work [15].

2.3. Characterization

X-ray diffraction (XRD) patterns were recorded on a Panalytical Empyrean multifunction X-ray diffractometer (Panalytical, Almelo, The Netherlands), equipped with a Cu K α radiation source and a three-dimensional (3D) PIXcel detector under a target voltage of 40 kV and current of 40 mA. A continuous scanning mode with a step size of 0.026° and a 30 s per step counting time was used to collect the patterns.

Transmission electron microscopy (TEM) measurements were carried out using an FEI Tecnai G2 F20 S-TWIN microscope (FEI, Hillsboro, OR, USA), which was operated at a 200 kV accelerating voltage. The samples were dispersed in ethanol and sonicated for 3 min, then a droplet of the sample suspension was dropped on a 200-mesh Cu grid coated with a carbon film, and the copper grid was left to stand for at least 10 min to prepare the TEM specimens.

Low-temperature nitrogen (N₂) adsorption–desorption isotherms were measured at a liquid nitrogen temperature using a Quantachrome Autosorb-iQ2-MP gas adsorption analyzer (Quantachrome, Boynton Beach, FL, USA). The samples were outgassed at 200 °C for 12 h under vacuum conditions before measurement. The multiple-point Brunauer–Emmett–Teller (BET) method was used to calculate the specific surface area, S_{BET} , of the sample from the N₂ adsorption data [33]. The total pore volume, V_{total} , was evaluated based on N₂ uptake at a relative pressure of ca. 0.99. The Barrett–Joyner–Halenda (BJH) method was used to derive the pore size distribution (PSD) curves of the samples from the adsorption branch of the isotherms [34].

2.4. Adsorption Experiments

The adsorption performance of the samples was studied by carrying out batch adsorption experiments. In a typical run, 50 mg of adsorbent was mixed with 20 mL of an I[−] solution at the specified concentration in a 50 mL centrifuge tube. For kinetics testing, the mixture in the centrifuge tube was shaken at a rate of 200 rpm in a platform shaker to ensure complete mixing. The adsorption time spanned from 10 min to 24 h. At the end of each time interval, each centrifuge tube was centrifuged and the supernatant was taken and passed through a 0.45 μm PTFE filter. The concentration of I[−] in the supernatant was determined using a Dionex ICS-90 Ion Chromatography (IC) system (Dionex, Sunnyvale, CA, USA) with an AG23 guard and AS23 analytical column. A 14 mM Na₂CO₃/1.75 mM NaHCO₃ solution was used as the eluent.

A very similar experimental procedure to the kinetics testing procedure was used to obtain the adsorption isotherms except the shaking time was fixed at 12 h. NaOH (0.1 mol/L) or HNO₃ (0.1 mol/L) was used to adjust the pH values of the suspensions. To study the effect of pH on adsorption, the initial pH value of the I[−] solution was adjusted to

approximately 4–10. The competitive adsorption of I^- by the nanomaterial was tested in the presence of high concentrations of other anion, such as Cl^- , Br^- , or SO_4^{2-} (1.5 mmol/L for I^- , 10 mmol/L for each competitive ion). All adsorption experiments were performed at room temperature, and blank experiments confirmed the absence of centrifuge tube wall adsorption and I^- loss due to volatilization.

The I^- removal efficiency, $E(\%)$, was calculated using the following equation:

$$E(\%) = [(C_0 - C_t)/C_0] \times 100 \quad (1)$$

where C_0 and C_t (mmol/L) are the concentrations of I^- in the reaction solution before and after adsorption for time t (h), respectively. The amount of I^- adsorbed per unit mass of the adsorbent at equilibrium, Q_e (mg/g), was calculated as follows:

$$Q_e = (C_0 - C_e) \times M/m \quad (2)$$

where C_e is the I^- concentration in the reaction solution at equilibrium, M is the molar mass of I^- , and m (g) is the amount of adsorbent in 1 L of I^- solution.

3. Results and Discussion

3.1. Characterization of the Hal Support and Hal/Ag₂O Nanomaterials

As revealed by the XRD pattern of Hal (Figure 1a), the main phase of Hal is 7Å-halloysite with the (001) reflection at 0.74 nm [35]. This Hal support was of high purity as there were no other reflections found from the XRD pattern. The diffraction pattern of Ag₂O-NPS exhibits distinct peaks at 26.76, 32.98, 38.29, 55.25, and 65.86° (2θ) (Figure 1b), which are consistent with the known diffraction pattern of silver oxide (Power Diffraction of File No. 41-1104), and are attributed to the (110), (111), (200), (220), and (311) reflections, respectively [36]. As calculated using the Scherrer formula in our previous work, Ag₂O-NPS has nanoscale dimensions, with an average particle size of 18.4 nm [15]. Figure 1c,d show the XRD patterns of the nanomaterials Hal/Ag₂O-1 and Hal/Ag₂O-2, respectively. The XRD pattern of Hal/Ag₂O-1 shows no obvious difference from that of Hal (Figure 1c), perhaps because the amount of Ag₂O in this sample is minor or the size of the Ag₂O particles is ultrafine. In the XRD pattern of Hal/Ag₂O-2 (Figure 1d), a new peak at 32.93° (2θ) appeared, and this peak can be attributed to the (111) reflection of Ag₂O. These results indicated the presence of silver oxide in the nanomaterials and that the amount of Ag₂O increased with the concentration of NaOH used in the preparation process.

The TEM image showed that the Hal particles possessed a typical cylindrical morphology and contained a transparent central area that runs longitudinally along the cylinder (Figure 2a), indicating that the halloysite particles were hollow and open ended. As obtained from the statistical measurements of several TEM images, the length of Hal varies from ca. 0.1 to 1.0 μ m, and the external diameter ranges from ca. 20 to 60 nm with the lumen diameter from ca. 9 to 22 nm. However, it should be noted that the validity of these morphological data is limited by the small number of particles measured in the TEM images.

The TEM images of the Hal/Ag₂O nanomaterials revealed that the Ag₂O nanoparticles were well dispersed on the surface of the halloysite nanotubes (Figure 2b–d). In contrast, pure Ag₂O nanoparticles tended to aggregate dramatically. For example, the Ag₂O-NPS used for comparison in this study agglomerated considerably, resulting in aggregates on the micrometer scale in size [15]. As shown by Figure 2b, a small amount of Ag₂O nanoparticles could be found on the outer surface of the Hal/Ag₂O-1 sample, and the average size of these Ag₂O nanoparticles is 6.07 ± 2.5 nm from the statistical measurement (inset of Figure 2b). For Hal/Ag₂O-2 prepared using 0.05 mol/L NaOH, the amount of Ag₂O nanoparticles on the surface of Hal increased significantly, and the average size of the Ag₂O nanoparticles increased slightly with a measured value of 8.04 ± 3.8 nm (Figure 2c,d). In our previous work, we found that the amount and size of the Ag₂O nanoparticles also changed with the concentration of silver nitrate [15]. These results indicated that

supporting Ag₂O nanoparticles on halloysite can significantly decrease its coaggregation and that the amount and size of the Ag₂O nanoparticles in the nanomaterials can be readily controlled by adjusting the preparation conditions, such as the concentration of NaOH or silver nitrate. In addition, a small amount of Ag₂O nanoparticles were also found in the lumen of the halloysite nanotubes (Figure 2d).

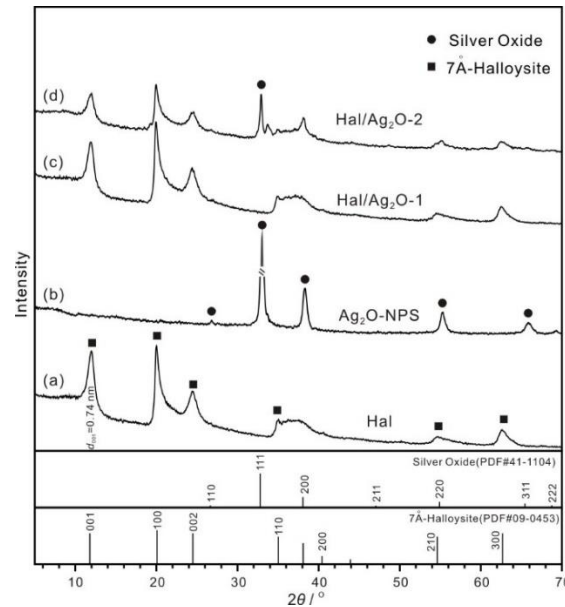


Figure 1. XRD patterns of (a) Hal, (b) Ag₂O-NPS, (c) Hal/Ag₂O-1, and (d) Hal/Ag₂O-2.

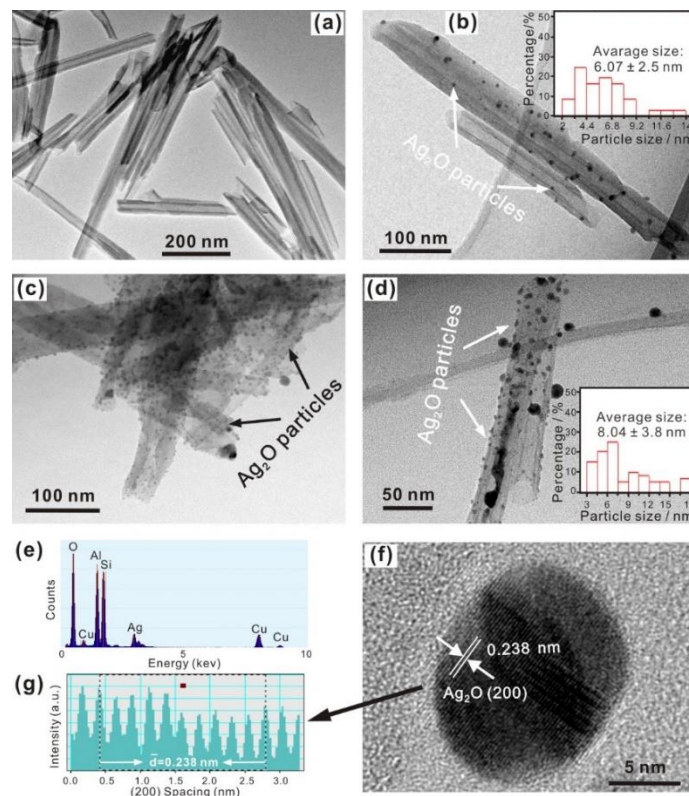


Figure 2. TEM images of (a) Hal, (b) Hal/Ag₂O-1 (inset is the histogram of Ag₂O particle sizes), (c,d) Hal/Ag₂O-2 (inset of Figure 2d is the histogram of Ag₂O particle sizes), an (e) EDS spectrum of Hal/Ag₂O-2, (f) HR-TEM image of a Ag₂O nanoparticle and (g) its integrated pixel intensities.

The EDS result (Figure 2e) for Hal/Ag₂O-2 confirms the presence of Ag and O elements in the nanomaterials, and the Ag₂O loading amounts in the nanomaterials were calculated using the Ag content from the EDS data, and are listed in Table 1. The fringes of the nanoparticles show a lattice spacing of 0.238 nm (Figure 2e,f), corresponding to the (200) plane of Ag₂O nanocrystals, which confirms that the nanoparticles on the surface of the sample are nanoscale Ag₂O particles.

Table 1. Porous structural data, and Ag and Ag₂O contents of the samples.

Samples	S _{BET} (m ² /g)	V _{total} (mL/g)	W _{Ag} (wt%) ¹	W _{Ag₂O} (wt%) ²
Hal	67.7	0.3344	–	–
Hal/Ag ₂ O-1	73.8	0.4003	0.64	0.69
Hal/Ag ₂ O-2	65.2	0.4146	5.92	6.36

¹ W_{Ag} (wt%), the Ag content of each Hal/Ag₂O composite, which is the average value of the Ag content from the EDS data. ² W_{Ag₂O} (wt%), the Ag₂O content of each Hal/Ag₂O composite, which was calculated from the W_{Ag} using the following equation: W_{Ag₂O} = W_{Ag} × (107.9 + 8)/107.9.

The N₂ adsorption–desorption isotherms and PSD curves of Hal and the Hal/Ag₂O nanomaterials are presented in Figure 3A,B, respectively. The isotherm shapes for Hal and both Hal/Ag₂O nanomaterials are similar, and can all be designated as type IV(a) with H3 hysteresis loops (Figure 3A), according to the updated classification of IUPAC [37]. This type of isotherm is characteristic of mesoporous structures. Compared with Hal, the hysteresis loops of both Hal/Ag₂O-1 and Hal/Ag₂O-2 were weakened. This result suggested that the mesopores in the nanomaterials were diminished compared with Hal.

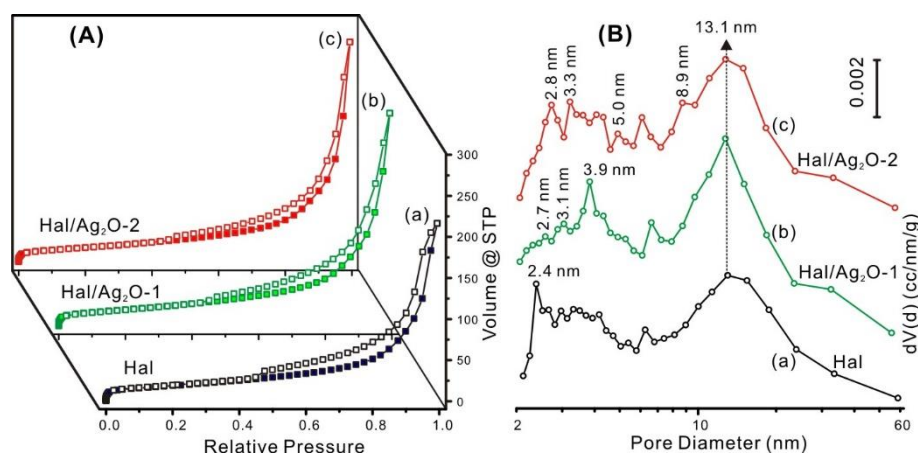


Figure 3. (A) N₂ adsorption–desorption isotherms of (a) Hal, (b) Hal/Ag₂O-1, and (c) Hal/Ag₂O-2; (B) PSD curves of (a) Hal, (b) Hal/Ag₂O-1, and (c) Hal/Ag₂O-2.

Two distinct mesoporous populations centered ca. 2.4 nm and 13.1 nm, respectively, were found in the PSD curve of Hal (Figure 3B(a)). The former was ascribed to the slit-shaped longitudinal pores, which were formed in the degassing process, and the latter was ascribed to the lumen of Hal [38]. For both nanomaterials, the PSD curve featured the mesopore populations attributable to the two types of pores mentioned above (Figure 3B(b,c)), but the distribution of the population at ca. 13.1 nm is narrower than that of Hal. This result may be explained by the occupation of the halloysite lumen by some Ag₂O particles, as indicated by the TEM images (Figure 2d). The mesopore populations from 3 to 9 nm in the nanomaterials arose from the interval space or stacking of Ag₂O particles on the surface of the halloysite, and these types of mesopores should be related to the content of Ag₂O. Compared with Hal/Ag₂O-1, Hal/Ag₂O-2 indeed has more pores ranging from 3 to 9 nm (Figure 3B(b,c)), and this is probably related to the higher content of Ag₂O in Hal/Ag₂O-2.

The S_{BET} of Hal is $67.7 \text{ m}^2/\text{g}$ (Table 1), which is slightly higher than the S_{BET} values of the halloysite samples studied in our previous works [15,31]. This result is due to the Hal nanotubes in this study exhibiting smaller dimensions. As shown in Table 1, Hal/Ag₂O-1 exhibited a higher S_{BET} value than Hal, and this is attributed to the presence of Ag₂O nanoparticles on halloysite. However, with the increase in the amount of Ag₂O nanoparticles, i.e., in the case of Hal/Ag₂O-2, a lower S_{BET} value than Hal was exhibited (Table 1). This result can be explained by two plausible reasons: 1) part of the lumen of the halloysite was occupied by some Ag₂O particles, resulting in a decreased S_{BET} for the nanomaterials; 2) the density of Ag₂O is greater than that of halloysite, and because S_{BET} is the surface area per gram of sample, the nanomaterial with more Ag₂O should have a lower S_{BET} . The V_{total} values of both nanomaterials are higher than that of Hal (Table 1), which is attributed to the presence of more interparticle pores in the nanomaterials.

3.2. Performance of the Hal/Ag₂O Nanomaterial for I[−] Adsorption

Due to its higher content of Ag₂O nanoparticles, Hal/Ag₂O-2 was selected for the I[−] adsorption tests in this study. It is worth noting that the I[−] adsorption performance of the prepared nanomaterials could vary with the content of Ag₂O; however, testing on this front will be studied as part of another investigation. As shown in Figure 4a, Hal/Ag₂O-2 adsorbed I[−] rapidly and the equilibrium can be reached within 100 min. This rapid adsorption of I[−] is attributed to the fact that most of the adsorption sites (Ag₂O nanoparticles) for I[−] existed on the outer surface of the nanomaterials, which is readily accessible to I[−], resulting in a rapid approach to the steady state.

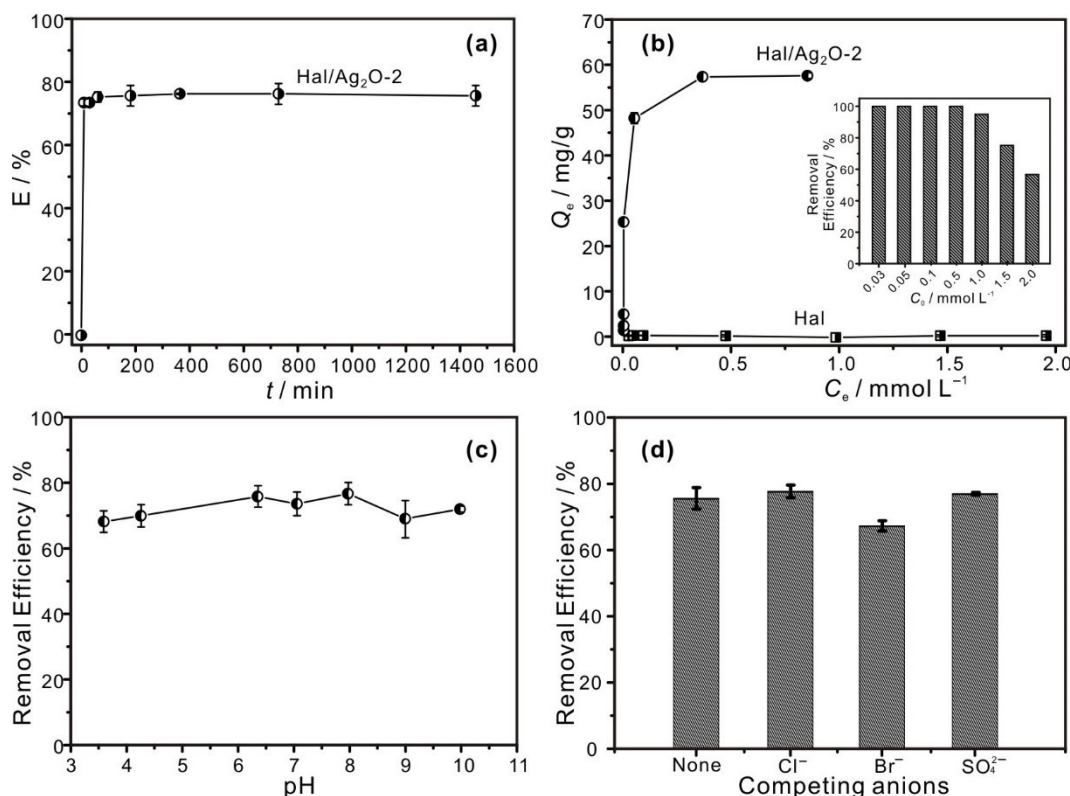


Figure 4. (a) Adsorption kinetics of I[−] on Hal/Ag₂O-2, (b) adsorption isotherms of I[−] on Hal and Hal/Ag₂O-2 (inset is the I[−] removal efficiency from the solutions with different initial concentrations of I[−] on Hal/Ag₂O-2), (c) the effect of pH on I[−] adsorption on Hal/Ag₂O-2, and (d) I[−] removal efficiency of Hal/Ag₂O-2 under competitive adsorption conditions.

The adsorption isotherm results revealed that Hal has negligible adsorption to I[−] with a Q_e of 0.4 mg/g while Hal/Ag₂O-2 has a much higher Q_e at 57.5 mg/g (Figure 4b),

which demonstrates that the introduction of Ag₂O nanoparticles in Hal dramatically increases its I[−] adsorption capacity. As shown in Table 2, the Q_e value of Hal/Ag₂O-2 is compared with other materials reported in the literature. It was found that the Q_e value for Hal/Ag₂O-2 is considerably higher than the values for black carbon [39], minerals (chrysotile, ferrihydrite, cuprite) [5,40,41], and layered double hydroxides [42] in the literature. However, Hal/Ag₂O-2 exhibited a lower adsorption capacity than the Ag₂O-grafted titanate nanolamina and nanofibers (Table 2), which is attributed to the lower Ag content in our material. As explained in the paper, the average weight percentage of Ag in the Ag₂O-grafted titanate nanolamina was as high as 40.3% [21], which is significantly higher than that in the materials prepared in this study (see Table 1). With a high adsorption capacity, in terms of removing radioactive iodine, 1 g of Hal/Ag₂O-2 was able to clean up 11.5 L of wastewater containing 5 ppm of radioactive iodine. To compare the I[−] adsorption efficiency of Hal/Ag₂O-2 with that of pure Ag₂O-NPS, the equilibrium adsorption capacity of Hal/Ag₂O-2 normalized to per unit mass of Ag₂O content, Q_{e-m}, was calculated according to Q_e and W_{Ag₂O} (Table 1) using the following equation:

$$Q_{e-m} = (Q_e - 0.4 \times (1 - (W_{Ag_2O}/100)))/(W_{Ag_2O}/100) \quad (3)$$

The obtained Q_{e-m} for Hal/Ag₂O-2 is 898.4 mg/g, which is significantly larger (4.4 times larger) than that for pure Ag₂O-NPS (201.9 mg/g [15]). This result is mainly attributed to the better dispersion of Ag₂O nanoparticles supported on halloysite. As shown by the inset of Figure 4b, Hal/Ag₂O-2 could remove 95% of I[−] from the solution when the initial I[−] concentration was 1.0 mmol/L, and 100% of I[−] could be removed when the initial I[−] concentration was 0.5 mmol/L or lower. These results strongly indicated that the prepared Hal/Ag₂O nanomaterial has the potential to be an efficient adsorbent for the removal of radioactive iodide from wastewater.

The pH shows no obvious effect on the I[−] removal efficiency in the range of ca. 4–10 (Figure 4c), suggesting that the adsorption process was not affected by hydrogen or hydroxide ions. As shown in Figure 4d, the I[−] removal efficiency of the Hal/Ag₂O nanomaterial waved slightly but remained high enough with the coexistence of Cl[−], Br[−], or SO₄^{2−}, even when the concentration of Cl[−], Br[−], or SO₄^{2−} was several times higher than that of I[−] (the concentration of I[−] was 1.5 mmol/L, and the concentration of each competitive ion was 10 mmol/L). This result suggests that the prepared nanomaterial possesses a high selectivity to I[−] adsorption. The lower Gibbs energy of the reaction of Ag₂O with I[−] than with the competing anions could explain the high selectivity of the nanomaterial; hence, the reaction of Ag₂O with I[−] is thermodynamically favored over that with Cl[−], Br[−], or SO₄^{2−} [21].

Table 2. Comparison of adsorption capacities of different adsorbents for I[−].

Adsorbents	I [−] Adsorption Capacities	Ref.
Hal/Ag ₂ O-2	57.7 mg/g	This work
Black carbon	~2 mg/g	[39]
Activated carbon	~12.7 mg/g	[17]
Chrysotile bundles	4.13 mg/g	[5]
Ferrihydrite	<0.127 mg/g	[40]
LDH	5.8 mg/g	[42]
Calcined LDH	96.1 mg/g	[42]
Cuprite (Cu ₂ O)	~0.15 mg/g	[41]
Ag ₂ O-grafted titanate nanolamina	431.8 mg/g	[21]
Ag ₂ O-grafted titanate nanofibers	381 mg/g	[22]

3.3. Adsorption Mechanism

The XRD patterns of Hal/Ag₂O-2 after adsorption of I[−] with low and high initial concentrations (0.5 and 2.0 mmol/L initial I[−] concentrations, respectively; solid/solution ratio 50 mg/20 mL; 12 h) are shown in Figure 5. The iodide-loaded samples were highlighted

with the suffix “-I_n”, where n indicates the initial concentration of I⁻ in mmol/L. After adsorption of I⁻, the (111) reflection of silver oxide at 32.93° (2θ) in Hal/Ag₂O-2 (Figure 5a) disappeared in both XRD patterns of Hal/Ag₂O-2-I_n (Figure 5b,c), indicating the diminishment or disappearance of Ag₂O in the nanomaterials. At the same time, new peaks at 22.27, 23.66, 39.18, and 46.17° (2θ) appeared in the XRD patterns of Hal/Ag₂O-2-I_n (Figure 5b,c), which can be attributed to the (100), (002), (110), and (112) reflections of iodargyrite. These results indicated that the Ag₂O nanoparticles in the nanomaterials reacted with I⁻ to form iodargyrite during the adsorption process. The weaker intensities of the peaks attributed to iodargyrite in Hal/Ag₂O-2-I_{0.5}, compared to that in Hal/Ag₂O-2-I_{2.0}, were because of the lower content of iodargyrite in Hal/Ag₂O-2-I_{0.5}. The adsorption mechanism could be surmised as the following reaction:

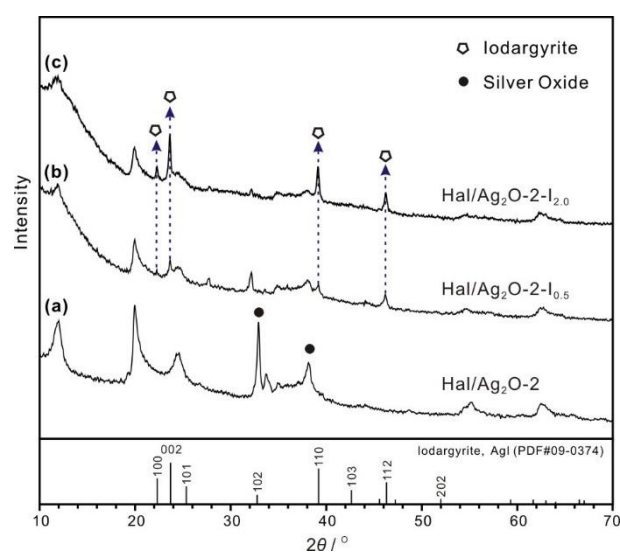
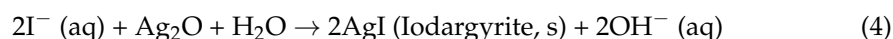


Figure 5. XRD patterns of (a) Hal/Ag₂O-2 and (b,c) Hal/Ag₂O-2 after adsorption of I⁻ at different concentrations.

According to this equation, the theoretical I⁻ adsorption capacity per gram of Ag₂O (4.3 mmol) should be 1095.8 mg (8.6 mmol). Therefore, the efficiency of Ag₂O utilized for the adsorption of I⁻, $E_{\text{Silver Oxide-U}}$ (%), of the samples can be calculated using the following equation: $E_{\text{Silver Oxide-U}} = Q_{\text{m-z}}/1095.8$. The calculated $E_{\text{Silver Oxide-U}}$ for pure Ag₂O-NPS and Hal/Ag₂O-2 is 18.4% and 82.0%, respectively. This result indicated that supporting Ag₂O nanoparticles on halloysite significantly increased the efficiency of Ag₂O utilized for the adsorption of I⁻.

Finally, because of the low solubility of the iodargyrite generated during the adsorption process, the Hal/Ag₂O nanomaterial prepared in this study could be an ideal material to solidify radioactive I⁻ in solution, retard its mobility, and further reduce its risk.

4. Conclusions

In this study, halloysite/Ag₂O nanomaterials were prepared by growing Ag₂O nanoparticles on the surface of nanotubular halloysite. The average sizes of the Ag₂O nanoparticles were 6.07 ± 2.5 nm and 8.04 ± 3.8 nm when the concentration of alkali solution was 0.01 and 0.05 mol/L, respectively. In the nanomaterials, the Ag₂O nanoparticles mainly exist on the external surface of the halloysite, with better dispersion and less coaggregation than the pure Ag₂O nanoparticles. The adsorption of I⁻ by the nanomaterial with 6.36% Ag₂O (Hal/Ag₂O-2) was rapid, and adsorption equilibrium was reached within 100 min. The adsorption capacity of I⁻ on Hal/Ag₂O-2 was 57.5 mg/g, which was significantly higher than that of halloysite (0.4 mg/g). The nanomaterial also showed a better adsorption

capacity per unit mass of Ag₂O than pure Ag₂O nanoparticles, and the efficiency of Ag₂O utilized for the adsorption of I[−] was 82% while that of the pure Ag₂O nanoparticles was as low as 18.4%, and this was attributed to the better dispersion of Ag₂O nanoparticles on halloysite. Moreover, Hal/Ag₂O-2 exhibited high selectivity for adsorption to I[−], and its I[−] removal efficiency was hardly affected by the coexistence of Cl[−], Br[−], or SO₄^{2−}. The initial pH of the I[−] solution also showed no obvious effect on the I[−] removal efficiency. Low-solubility iodargyrite was generated during the adsorption process. These results indicated that the prepared Hal/Ag₂O nanomaterial could be a new and efficient adsorbent capable of the adsorption of radioactive I[−] from aqueous solution.

Author Contributions: Conceptualization, W.Y. (Wenbin Yu) and Q.W.; methodology, W.Y. (Wenlin Yu); formal analysis, X.N. and Z.Q.; investigation, W.Y. (Wenlin Yu) and Q.D.; writing—original draft preparation, W.Y. (Wenlin Yu); writing—review and editing, W.Y. (Wenbin Yu), Q.W., and X.C.; supervision, Q.W. and X.C.; funding acquisition, W.Y. (Wenbin Yu) and Q.W. All authors have read and agreed to the published version of the manuscript.

Funding: This research was funded by the National Natural Science Foundation of China, grant numbers 42072057 and 41872046, and the Guizhou Provincial Science and Technology Project, grant number ZK[2021]ZD043.

Data Availability Statement: The data presented in this study are available on request from the corresponding author.

Acknowledgments: The authors thank Shirong Liu of the Institute of Geochemistry, Chinese Academy of Science for collecting TEM images and X-ray EDS maps. The authors also thank the editor and the anonymous reviewers for their constructive comments and suggestions.

Conflicts of Interest: The authors declare no conflict of interest.

References

1. Wang, X.; Chen, L.; Wang, L.; Fan, Q.; Pan, D.; Li, J.; Chi, F.; Xie, Y.; Yu, S.; Xiao, C.; et al. Synthesis of novel nanomaterials and their application in efficient removal of radionuclides. *Sci. China Chem.* **2019**, *62*, 933–967. [[CrossRef](#)]
2. Hong, S.; Um, W. Top-Down Synthesis of NaP Zeolite from Natural Zeolite for the Higher Removal Efficiency of Cs, Sr, and Ni. *Minerals* **2021**, *11*, 252. [[CrossRef](#)]
3. Kaplan, D.I.; Serne, R.J.; Parker, K.E.; Kutnyakov, I.V. Iodide Sorption to Subsurface Sediments and Illitic Minerals. *Environ. Sci. Technol.* **2000**, *34*, 399–405. [[CrossRef](#)]
4. Fuge, R.; Johnson, C.C. Iodine and human health, the role of environmental geochemistry and diet, a review. *Appl. Geochem.* **2015**, *63*, 282–302. [[CrossRef](#)]
5. Yu, W.; Xu, H.; Roden, E.E.; Wan, Q. Efficient adsorption of iodide from water by chrysotile bundles with wedge-shaped nanopores. *Appl. Clay Sci.* **2019**, *183*, 105331. [[CrossRef](#)]
6. Choung, S.; Kim, M.; Yang, J.S.; Kim, M.G.; Um, W. Effects of Radiation and Temperature on Iodide Sorption by Surfactant-Modified Bentonite. *Environ. Sci. Technol.* **2014**, *48*, 9684–9691. [[CrossRef](#)]
7. Theiss, F.L.; Ayoko, G.A.; Frost, R.L. Iodide removal using LDH technology. *Chem. Eng. J.* **2016**, *296*, 300–309. [[CrossRef](#)]
8. Lee, S.-H.; Takahashi, Y. Selective immobilization of iodide onto a novel bismuth-impregnated layered mixed metal oxide: Batch and EXAFS studies. *J. Hazard. Mater.* **2020**, *384*, 121223. [[CrossRef](#)]
9. Yoshida, S.; Muramatsu, Y.; Uchida, S. Studies on the sorption of I[−] (iodide) and IO₃[−] (iodate) onto Andosols. *Water Air Soil Pollut.* **1992**, *63*, 321–329. [[CrossRef](#)]
10. Dai, J.L.; Zhang, M.; Hu, Q.H.; Huang, Y.Z.; Wang, R.Q.; Zhu, Y.G. Adsorption and desorption of iodine by various Chinese soils: II. Iodide and iodate. *Geoderma* **2009**, *153*, 130–135. [[CrossRef](#)]
11. Wu, H.; Wu, Y.; Chen, Z.; Wei, Y.Z. Adsorption behaviors of iodide anion on silver loaded macroporous silicas. *Nucl. Sci. Tech.* **2015**, *26*, 30301.
12. Bichsel, Y.; von Gunten, U. Oxidation of Iodide and Hypoiodous Acid in the Disinfection of Natural Waters. *Environ. Sci. Technol.* **1999**, *33*, 4040–4045. [[CrossRef](#)]
13. Liu, S.; Wang, N.; Zhang, Y.; Li, Y.; Han, Z.; Na, P. Efficient removal of radioactive iodide ions from water by three-dimensional Ag₂O–Ag/TiO₂ composites under visible light irradiation. *J. Hazard. Mater.* **2015**, *284*, 171–181. [[CrossRef](#)] [[PubMed](#)]
14. Tanno, K.; Liao, X.; Kurosawa, F. Electrolysis of ammonium iodide solution in a Na₂CO₃ I₂ hybrid cycle. *Int. J. Hydrog. Energy* **1986**, *11*, 463–469. [[CrossRef](#)]
15. Yu, W.; Wan, Q.; Tan, D.; Yang, S.; Qin, Z.; Nie, X. Removal of iodide from water using halloysite/Ag₂O composites as efficient adsorbent. *Appl. Clay Sci.* **2021**, *213*, 106241. [[CrossRef](#)]

16. Talan, D.; Huang, Q. Separation of Radionuclides from a Rare Earth-Containing Solution by Zeolite Adsorption. *Minerals* **2021**, *11*, 20. [[CrossRef](#)]
17. Hoskins, J.S.; Karanfil, T.; Serkiz, S.M. Removal and Sequestration of Iodide Using Silver-Impregnated Activated Carbon. *Environ. Sci. Technol.* **2002**, *36*, 784–789. [[CrossRef](#)] [[PubMed](#)]
18. Miller, A.; Krulichak, J.; Mills, M.; Wang, Y. Iodide uptake by negatively charged clay interlayers? *J. Environ. Radioact.* **2015**, *147*, 108–114. [[CrossRef](#)] [[PubMed](#)]
19. Mao, P.; Qi, B.; Liu, Y.; Zhao, L.; Jiao, Y.; Zhang, Y.; Jiang, Z.; Li, Q.; Wang, J.; Chen, S.; et al. AgII doped MIL-101 and its adsorption of iodine with high speed in solution. *J. Solid State Chem.* **2016**, *237*, 274–283. [[CrossRef](#)]
20. Liu, Y.; Gu, P.; Jia, L.; Zhang, G. An investigation into the use of cuprous chloride for the removal of radioactive iodide from aqueous solutions. *J. Hazard. Mater.* **2016**, *302*, 82–89. [[CrossRef](#)]
21. Bo, A.; Sarina, S.; Zheng, Z.; Yang, D.; Liu, H.; Zhu, H. Removal of radioactive iodine from water using Ag₂O grafted titanate nanolamina as efficient adsorbent. *J. Hazard. Mater.* **2013**, *246*, 199–205. [[CrossRef](#)] [[PubMed](#)]
22. Yang, D.; Sarina, S.; Zhu, H.; Liu, H.; Zheng, Z.; Xie, M.; Smith, S.V.; Komarneni, S. Capture of radioactive cesium and iodide ions from water by using titanate nanofibers and nanotubes. *Angew. Chem.* **2011**, *123*, 10782–10786. [[CrossRef](#)]
23. Joussein, E.; Petit, S.; Churchman, J.; Theng, B.; Righi, D.; Delvaux, B. Halloysite clay minerals—a review. *Clay Miner.* **2005**, *40*, 383–426. [[CrossRef](#)]
24. Yuan, P.; Southon, P.D.; Liu, Z.; Green, M.E.; Hook, J.M.; Antill, S.J.; Kepert, C.J. Functionalization of halloysite clay nanotubes by grafting with γ -aminopropyltriethoxysilane. *J. Phys. Chem. C* **2008**, *112*, 15742–15751. [[CrossRef](#)]
25. Yuan, P.; Tan, D.; Annabi-Bergaya, F. Properties and applications of halloysite nanotubes: Recent research advances and future prospects. *Appl. Clay Sci.* **2015**, *112–113*, 75–93. [[CrossRef](#)]
26. Rawtani, D.; Agrawal, Y.K. Halloysite as support matrices: A review. *Emerging Mater. Res.* **2012**, *1*, 212–220. [[CrossRef](#)]
27. Wang, J.; Wu, S.; Zhang, W.; Wang, H.; Zhang, P.; Jin, B.; Wei, C.; Guo, R.; Miao, S. Selective decorating Ag and MnOx nanoparticles on halloysite and used as micromotor for bacterial killing. *Appl. Clay Sci.* **2022**, *216*, 106352. [[CrossRef](#)]
28. Ouyang, J.; Guo, B.B.; Fu, L.J.; Yang, H.M.; Hu, Y.H.; Tang, A.D.; Long, H.M.; Jin, Y.L.; Chen, J.; Jiang, J.L. Radical guided selective loading of silver nanoparticles at interior lumen and out surface of halloysite nanotubes. *Mater. Des.* **2016**, *110*, 169–178. [[CrossRef](#)]
29. Yu, J.; Niedenthal, W.; Smarsly, B.M.; Natile, M.M.; Huang, Y.; Carraro, M. Au nanoparticles supported on piranha etched halloysite nanotubes for highly efficient heterogeneous catalysis. *Appl. Surf. Sci.* **2021**, *546*, 149100. [[CrossRef](#)]
30. Papoulis, D.; Komarneni, S.; Panagiotaras, D.; Stathatos, E.; Toli, D.; Christoforidis, K.C.; Fernández-García, M.; Li, H.; Yin, S.; Sato, T.; et al. Halloysite–TiO₂ nanocomposites: Synthesis, characterization and photocatalytic activity. *Appl. Catal. B* **2013**, *132–133*, 416–422. [[CrossRef](#)]
31. Yu, W.; Xu, H.; Tan, D.; Fang, Y.; Roden, E.E.; Wan, Q. Adsorption of iodate on nanosized tubular halloysite. *Appl. Clay Sci.* **2020**, *184*, 105407. [[CrossRef](#)]
32. Ikari, M.; Matsui, Y.; Suzuki, Y.; Matsushita, T.; Shirasaki, N. Removal of iodide from water by chlorination and subsequent adsorption on powdered activated carbon. *Water Res.* **2015**, *68*, 227–237. [[CrossRef](#)] [[PubMed](#)]
33. Brunauer, S.; Emmett, P.H.; Teller, E. Adsorption of gases in multimolecular layers. *J. Am. Chem. Soc.* **1938**, *60*, 309–319. [[CrossRef](#)]
34. Barrett, E.P.; Joyner, L.G.; Halenda, P.P. The determination of pore volume and area distributions in porous substances. I. Computations from nitrogen isotherms. *J. Am. Chem. Soc.* **1951**, *73*, 373–380. [[CrossRef](#)]
35. Tan, D.Y.; Yuan, P.; Annabi-Bergaya, F.; Yu, H.G.; Liu, D.; Liu, H.M.; He, H.P. Natural halloysite nanotubes as mesoporous carriers for the loading of ibuprofen. *Microporous Mesoporous Mater.* **2013**, *179*, 89–98. [[CrossRef](#)]
36. Welton-Holzer, J.; McCarthy, G.; Grier, D. *Grant-in-Aid, I. North Dakota State University*; ICDD Grant-in-Aid: Fargo, ND, USA, 1989.
37. Thommes, M.; Kaneko, K.; Neimark, A.V.; Olivier, J.P.; Rodriguez-Reinoso, F.; Rouquerol, J.; Sing, K.S.W. Physisorption of gases, with special reference to the evaluation of surface area and pore size distribution (IUPAC Technical Report). *Pure Appl. Chem.* **2015**, *87*, 1051–1069. [[CrossRef](#)]
38. Ouyang, J.; Mu, D.; Zhang, Y.; Yang, H. Mineralogy and Physico-Chemical Data of Two Newly Discovered Halloysite in China and Their Contrasts with Some Typical Minerals. *Minerals* **2018**, *8*, 108. [[CrossRef](#)]
39. Choung, S.; Um, W.; Kim, M.; Kim, M.G. Uptake Mechanism for Iodine Species to Black Carbon. *Environ. Sci. Technol.* **2013**, *47*, 10349–10355. [[CrossRef](#)]
40. Yu, Z.; Warner, J.A.; Dahlgren, R.A.; Casey, W.H. Reactivity of iodide in volcanic soils and noncrystalline soil constituents. *Geochim. Cosmochim. Acta* **1996**, *60*, 4945–4956. [[CrossRef](#)]
41. Lefèvre, G.; Walcarius, A.; Ehrhardt, J.J.; Bessière, J. Sorption of Iodide on Cuprite (Cu₂O). *Langmuir* **2000**, *16*, 4519–4527. [[CrossRef](#)]
42. Liang, L.; Li, L. Adsorption behavior of calcined layered double hydroxides towards removal of iodide contaminants. *J. Radioanal. Nucl. Chem.* **2007**, *273*, 221–226. [[CrossRef](#)]